The Energetics of the Lagrangian Evolution of Tropical Convective Systems

HIROHIKO MASUNAGA[a] AND HANII TAKAHASHI[b]

[a] *Institute for Space-Earth Environmental Research, Nagoya University, Nagoya, Japan*
[b] *Jet Propulsion Laboratory, California Institute of Technology, Pasadena, California*

(Manuscript received 22 August 2023, in final form 17 January 2024, accepted 26 February 2024)

ABSTRACT: The convective life cycle is often conceptualized to progress from congestus to deep convection and develop further to stratiform anvil clouds, accompanied by a systematic change in the vertical structure of vertical motion. This archetype scenario has been developed largely from the Eulerian viewpoint, and it has yet to be explored whether the same life cycle emerges itself in a moving system tracked in the Lagrangian manner. To address this question, Lagrangian tracking is applied to tropical convective systems in combination with a thermodynamic budget analysis forced by satellite-retrieved precipitation and radiation. A new method is devised to characterize the vertical motion profiles in terms of the column import or export of moisture and moist static energy (MSE). The bottom-heavy, midheavy, and top-heavy regimes are identified for every $1° \times 1°$ grid pixel accompanying tracked precipitation systems, making use of the diagnosed column export/import of moisture and MSE. The major findings are as follows. The Lagrangian evolution of convective systems is dominated by a state of dynamic equilibrium among different convective regimes rather than a monotonic progress from one regime to the next. The transition from the bottom-heavy to midheavy regimes is fed with intensifying precipitation presumably owing to a negative gross moist stability (GMS) of the bottom-heavy regime, whereas the transition from the midheavy to top-heavy regimes dissipates the system. The bottom-heavy to midheavy transition takes a relaxation time of about 5 h in the equilibrating processes, whereas the relaxation time is estimated as roughly 20 h concerning the midheavy to top-heavy transition.

KEYWORDS: Tropics; Convection; Convective-scale processes; Satellite observations

1. Introduction

In the general context of fluid dynamics, convection is often treated as a bulk ensemble of unresolved turbulent eddies while their net effect on the heat and/or momentum budget on resolved scales is explicitly analyzed. Atmospheric moist convection serves as an example in that it is often argued to be an implicit ingredient in driving the tropical atmosphere in a quasi-equilibrium thermodynamic state (e.g., Arakawa and Schubert 1974; Emanuel et al. 1994). Nonetheless, moist convection is more than unresolved turbulence. Precipitating clouds are occasionally developed into a long-lived, organized convective system, with its internal structure changing systematically over time during the life cycle. The structural evolution of mesoscale convective systems (MCSs) typically begins with an intensifying stage characterized by cumulus congestus clouds growing into deeper convective towers, followed by a mature stage consisting of deep convective cores and extensive stratiform anvils (Leary and Houze 1979).

This well-established picture of convective evolution is known to prevail over a broad range of spatial and temporal scales across the hierarchy of tropical convective disturbances (Mapes et al. 2006). Such examples include the quasi-2-day wave (Takayabu et al. 1996), the convectively coupled Kelvin wave (Straub and Kiladis 2003), and the Madden–Julian oscillation (Lin and Johnson 1996). Congestus clouds, deep convection, and stratiform anvils each have distinct heating profiles, giving rise to a bottom-heavy or top-heavy thermal forcing to the atmosphere depending on the proportion at which convective/stratiform rain contributes to the total precipitation (Schumacher et al. 2004; Back et al. 2017). These impacts of heating profiles on the environment and the resulting feedback on convective dynamics have been incorporated into a school of theory on convectively coupled equatorial waves (Mapes 2000; Khouider and Majda 2006; Kuang 2008).

It should be noted that the archetype of the convective life cycle as illustrated above has been conceptualized largely from the Eulerian viewpoint, although not without exception (e.g., Hannah et al. 2016). In reality, MCSs move around at a speed of around 10 m s^{-1} at tropical latitudes (Feng et al. 2021), implying that they migrate over a distance of a few hundred kilometers during a time span of 10 h. Given that a lifetime of 10 h and a size of $O(100)$ km fall within a typical parameter range of organized convective systems (e.g., Chen and Houze 1997), an MCS is well capable of traveling beyond its own horizontal extent in the course of its life cycle. It follows that the Lagrangian frame is no less appropriate than the Eulerian for tracking the evolving structure of MCSs.

Automated methods to track convective systems in a sequence of satellite images have been developed over decades. A prototype algorithm dates back to the early years of geostationary Earth-orbiting (GEO) satellites (Woodley et al. 1980), which was later refined by subsequent studies (Williams and Houze 1987; Mapes and Houze 1993; Machado et al. 1998). A

Supplemental information related to this paper is available at the Journals Online website: https://doi.org/10.1175/JAS-D-23-0141.s1.

Corresponding author: Hirohiko Masunaga, masunaga@nagoya-u.jp

DOI: 10.1175/JAS-D-23-0141.1

number of novel approaches have emerged in recent years (Futyan and Del Genio 2007; Feng et al. 2012; Fiolleau and Roca 2013a,b; Heikenfeld et al. 2019; Takahashi et al. 2021, among others), opening pathways to a spectrum of new applications of the Lagrangian cloud tracking with a focus on radiation (Feng et al. 2011; Bouniol et al. 2016, 2021), precipitation (Feng et al. 2021; Takahashi et al. 2021), high clouds (Luo and Rossow 2004), and convective dynamics (Takahashi and Luo 2014; Elsaesser et al. 2022).

Our central interest in this study lies not in the cloud-scale evolution of an individual MCS but in the dynamic processes governing the interactions between the atmosphere and an ensemble of clouds that reside in it. More specifically, the focus is put on how a convecting atmospheric column gains or loses moisture and moist static energy (MSE) and how it evolves over the Lagrangian life cycle of convective systems. To this end, the composite life cycle of convection constructed from a convection tracking dataset is combined with a moisture and MSE budget analysis forced by satellite-retrieved precipitation and radiation. A precipitation-based tracking method is employed in order to capture congestus rainfall that would be difficult to detect with infrared-based tracking. On the other hand, the dissipating stage of MCS accompanied only by nonprecipitating anvil clouds would be left out of the analysis.

Of particular interest is whether the well-known Eulerian scenario emerges itself in the Lagrangian framework as well. As will turn out, the Lagrangian evolution of tropical organized convection is quite different from what one might expect from conventional knowledge. Our findings are detailed below, following an outline of the Lagrangian tracking database and the methodology of thermodynamic budget analysis.

2. Lagrangian tracking of convective systems

a. IMERG-CT

The present work adopts the Integrated Multisatellite Retrieval for GPM (IMERG)-based Convection Tracking (IMERG-CT) dataset (Takahashi et al. 2021). IMERG, a half-hourly, $0.1^\circ \times 0.1^\circ$ global precipitation product, provides surface precipitation estimates derived from a constellation of satellite passive microwave observations that are compiled with GEO and LEO infrared measurements and are adjusted to rain gauge network data over land (Huffman et al. 2020). Lagrangian tracking is applied to the IMERG V06 precipitation, which is a unique signature of IMERG-CT because most of the existing cloud-tracking methods are built upon infrared imagery alone. The caveat is that IMERG precipitation is not entirely independent of satellite infrared measurements, which the IMERG algorithm relies on to fill in gaps in sporadic passive-microwave retrievals. Nevertheless, IMERG-CT offers an advantage to this work since precipitation is a key variable in the MSE budget analysis outlined later. In the original IMERG-CT algorithm, an additional constraint was applied that infrared brightness temperature should decrease beyond 245 K at least one time during the lifetime. This condition does not significantly affect the results and is no longer applied to this study.

TABLE 1. Number of IMERG-CT samples sorted by lifetime. Each PC family (or life cycle) is counted as a single sample.

Lifetime (h)	Number of samples
0.5–3	205 514
3–6	64 373
6–9	18 164
9–12	7313
12–15	3811
15–18	2010
18–21	1148
21–24	712

The algorithm to produce the IMERG-CT dataset works as follows. First, a precipitation core (PC) is identified as a contiguous area of considerable precipitation ($\geq$5 mm h^{-1}). PCs are tracked in a manner based on 3D (i.e., 2D in space and 1D in time) 10-connectivity segmentation as devised by Fiolleau and Roca (2013a): If the eight pixels surrounding a reference PC pixel and the two temporally adjacent pixels (one before and another after) all meet the PC criterion, these 10 pixels are considered to be part of the same PC family as the reference pixels. Repeating this procedure to all qualifying pixels until unable to continue any further, one eventually finds a 3D structure of pixels connecting together in space and time, which as a whole is recorded to constitute a single family of PCs. This PC family defines the life cycle of a convective system, which potentially contains the merging and/or splitting of clouds at some point of the evolution.

Precipitation systems (PSs) are then defined on a snapshot-by-snapshot basis by extending the search for contiguous precipitating pixels beyond each PC until a lowered threshold of 0.5 mm h^{-1} is met. By construction, any PS must enclose at least one PC in itself, with the possibility that multiple PCs may be embedded when PSs sought around different PCs in the neighborhood end up in the same system. Each PS is thought of as a member of the same family as its "seeder PC" belongs to. A more thorough description of the algorithm is found in Takahashi et al. (2021).

b. Composite life cycle of PSs

A large population of PC/PS families are collected from the IMERG-CT database for finding the general properties of convective systems and their evolution over life cycle. The period analyzed is 2 years from 1 January 2007 to 31 December 2008, with the study area being tropical latitudes between 20°S and 20°N across all longitudes over both ocean and land. The size of IMERG-CT samples is listed in Table 1, where the population of PC families is broken down by lifetime every 3 h. It is noted that a lifetime shorter than 30 min and a PC area smaller than 400 km^2, hardly resolved given the native resolution of IMERG (half-hourly and 0.1°), are discarded from the analysis. It is evident from Table 1 that the samples become increasingly fewer as the lifetime increases. Lifetimes longer than 24 h are not included in the analysis

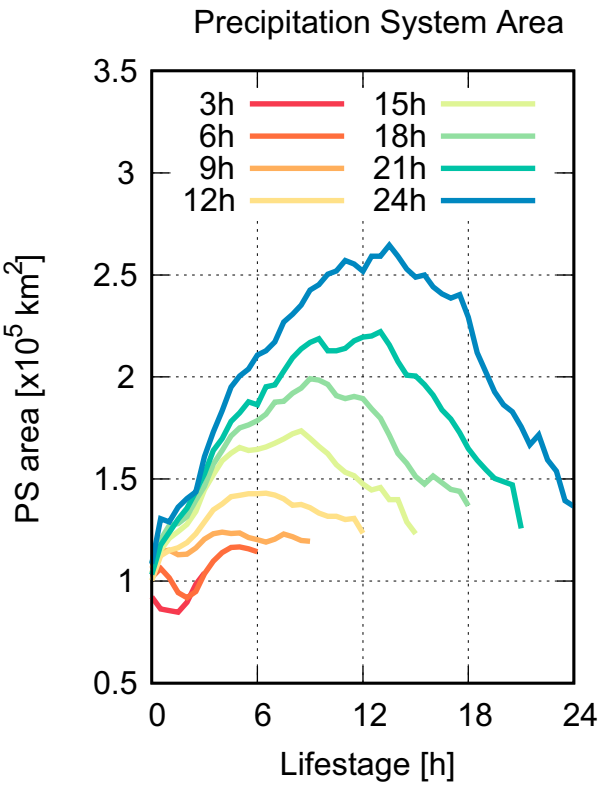

FIG. 1. Composite life cycle of PS area size sorted by lifetime as indicated in the inset legend, where 3–6 h is labeled as "6h" as an example.

because statistical robustness is difficult to ensure for exceptionally long-lived systems.

A set of composite life cycles are constructed by averaging all the detected PC/PS families at each life stage. This is done separately for different lifetimes as classified in Table 1. Figure 1 shows the temporal evolution of the PS area throughout the course of life cycle. The PS area for long-lived systems grows until it reaches a maximum and then shrinks over time, with the maximum being larger and later as lifetime is elongated. This is a signature known in the literature (e.g., Machado et al. 1998; Inoue et al. 2009). Short-lived systems are not precisely in line with this rule of thumb for unknown reasons. PSs are found to be typically on the order of 10^5 km^2 in area or a few hundred kilometers in length scale.

The composite life cycle of precipitation is presented in Fig. 2. The precipitation averaged over PS (Fig. 2a) and the maximum precipitation within PS (Fig. 2b) each follow a quasi-symmetric bell-shaped curve over life cycle resembling the areal evolution shown above (Fig. 1). The bell-like symmetry, however, breaks down especially for longer-lived PSs when the maximum and average precipitations are combined into their ratio, which steeply rises during the first few hours regardless of lifetime (Fig. 2c). A notable feature salient for long-lived systems is that the maximum-to-average precipitation ratio exhibits an extended period of plateau during the hours of enhanced precipitation. It is noted that Fig. 2 would remain qualitatively unchanged if plotted separately for the PSs over ocean and those over land, although the land composite is somewhat noisy due to a small sample size (see Fig. S1 in the online supplemental material).

The plateau came as a surprise at first to the authors, as there seemed no physical reason. What gives rise to this plateau, then? An explanation does exist, however, to qualitatively interpret this behavior. Let us consider a simple conceptual model of MCS comprising an intensely precipitating convective core and a lightly raining stratiform anvil,

$$\overline{P} = f_c P_c + (1 - f_c) P_s, \tag{1}$$

where $\overline{P}$ is the system-averaged precipitation, P_c and P_s are convective and stratiform precipitation, respectively, and f_c is the fractional cover of the convective core. Since the system-maximum precipitation occurs in a convective area and hence P_c may be considered to vary roughly in proportional to the maximum precipitation in this simplistic model, the maximum-to-average precipitation ratio r_P is

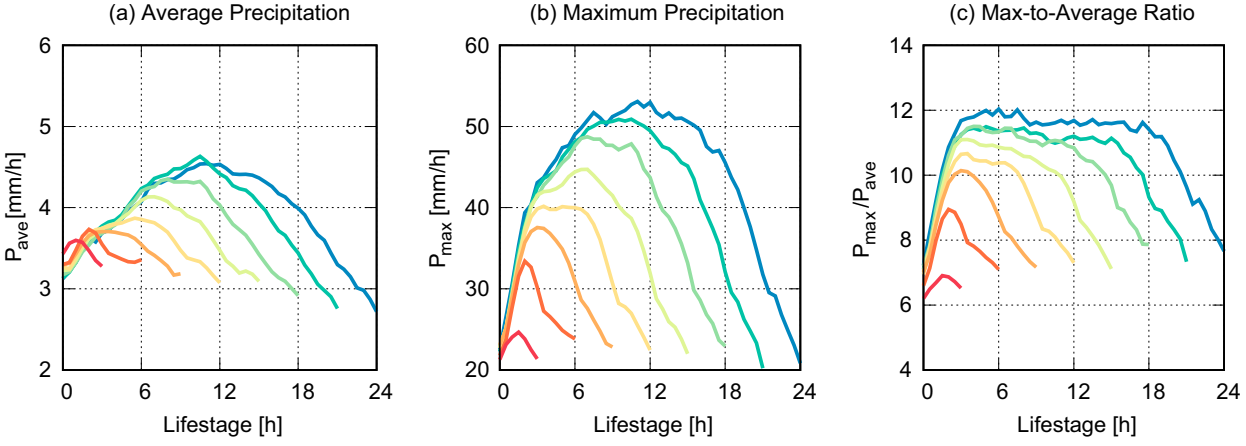

FIG. 2. Lifetime-sorted composite life cycle of (a) PS-averaged precipitation, (b) PS-maximum precipitation, and (c) the ratio of the maximum precipitation to the average precipitation.

$$r_P \propto \frac{P_c}{\overline{P}} = \left[f_c + (1 - f_c)\frac{P_s}{P_c} \right]^{-1}. \quad (2)$$

For a well-developed MCS where P_c well exceeds P_s, Eq. (2) can be simplified further into

$$r_P \propto \frac{1}{f_c}. \quad (3)$$

Figure 2c and Eq. (3) together lead to a working hypothesis that some mechanism might be at work to keep f_c nearly constant, as necessitated to account for the plateau of r_P, throughout the mature stage of long-lived convective systems.

The initial rise and subsequent plateau of r_P are consistent with Elsaesser et al. (2022), who showed that f_c from the Global Precipitation Mission (GPM) Dual-frequency Precipitation Radar (DPR) product decreases to a minimum toward the mature stage and stays nearly constant in the rest of evolution. This unexpected behavior suggests a mechanism for the Lagrangian convective evolution that has yet to be explored in depth. To this end, we next examine the dynamic processes governing the Lagrangian life cycle of convective systems. The above hypothesis will be revisited in light of the analysis results in section 5.

3. Diagnosis method of convective regimes

A useful approach to look into the dynamics of moist convection is to examine the column processes driven by vertical motion (Chikira 2014) and the associated variability in the moisture and MSE budget. A bulk portion of moisture resides in the lower troposphere, so that an upward motion at low levels, associated with a lower-tropospheric convergence, always imports moisture into the atmospheric column regardless of the depth of ascent. In contrast, MSE is exported out of the column by a top-heavy ascent, while MSE is exported only to a lesser extent or can be even imported when the ascent is bottom-heavy because MSE increases toward both the surface and tropopause from a midtropospheric minimum in the typical tropical sounding. The fact that the column MSE variability is sensitive to the vertical profile of vertical motion has been exploited in investigating the large-scale dynamics associated with the convective life cycle (e.g., Masunaga and L'Ecuyer 2014; Inoue and Back 2015, 2017).

A new analysis strategy is devised in this study, loosely built upon the moisture and MSE budget diagnosis of Masunaga and L'Ecuyer (2014), but readjusted, so it fits the Lagrangian tracking. The physical basis of the algorithm is first outlined.

a. Formulation of diagnostic equations

The methodological basis is founded on the vertically integrated moisture and MSE budget equations,

$$D_t\langle q \rangle + \langle \omega \partial_p q \rangle = E - P, \quad (4)$$

$$D_t\langle h \rangle + \langle \omega \partial_p h \rangle = S + LE + \langle Q_R \rangle, \quad (5)$$

respectively, where

$$D_t \equiv \partial_t + \mathbf{v}_H \cdot \nabla_H$$

is the Lagrangian derivative operator with the subscript H referring to the horizontal component,

$$\langle \cdots \rangle \equiv \int \cdots \frac{dp}{g}$$

is the vertical integral to the whole thickness of the atmosphere, q is the vapor mixing ratio, h is the MSE per unit mass, ω is the vertical p velocity, E is the surface evaporation flux, P is the precipitation, S is the sensible heat flux, Q_R is the radiative heating rate per unit mass, and L is the specific latent heat of vaporization. The Lagrangian framework is adopted because it is better suited for the convection-tracking analysis than the Eulerian approach. It is worth noting that the horizontal advection term is combined into the Lagrangian derivative and does not explicitly appear in the current formulation.

For the sake of putting focus on the convection-induced variability, the clear-sky component is subtracted from the all-sky counterpart for all atmospheric and surface variables and is denoted by prime as, for instance,

$$\langle Q_R \rangle' \equiv \langle Q_R \rangle - \langle Q_R \rangle_{\text{clear}}, \quad (6)$$

where $\langle Q_R \rangle'$ defines the column-integrated atmospheric cloud radiative effect (ACRE). The clear sky is assumed to be in its own balanced state,

$$D_t\langle q \rangle_{\text{clear}} + \langle \omega \partial_p q \rangle_{\text{clear}} = E_{\text{clear}},$$

$$D_t\langle h \rangle_{\text{clear}} + \langle \omega \partial_p h \rangle_{\text{clear}} = S_{\text{clear}} + LE_{\text{clear}} + \langle Q_R \rangle_{\text{clear}}.$$

Convective dynamics is defined as an anomaly against this hypothetical clear sky representing the local background state with a weak subsidence. Equations (4) and (5) are rewritten by subtracting the clear-sky component as

$$D_t\langle q \rangle' + \langle \omega \partial_p q \rangle' \approx -P, \quad (7)$$

$$D_t\langle h \rangle' + \langle \omega \partial_p h \rangle' \approx \langle Q_R \rangle'. \quad (8)$$

Here, E' and S' have been omitted because evaporation flux and sensible heat flux are much less sensitive to cloudiness than precipitation and radiation. Precipitation is absent in clear skies, so $P' = P$ at all times. Equations (7) and (8) claim that the moisture and MSE budget equations for the primed variables are forced by precipitation and the column-integrated ACRE, respectively. As evident from its definition, ACRE refers to the effect on the atmosphere alone in this paper and should not be confused with the cloud forcing to the whole Earth's system including the surface.

The vertical motion ω is decomposed into the first two baroclinic modes with all higher-order modes ignored,

$$\omega = \omega_1 + \omega_2, \quad (9)$$

where half a wavelength (a full wavelength) is equivalent to the depth of the troposphere for ω_1 (ω_2). The sign and relative

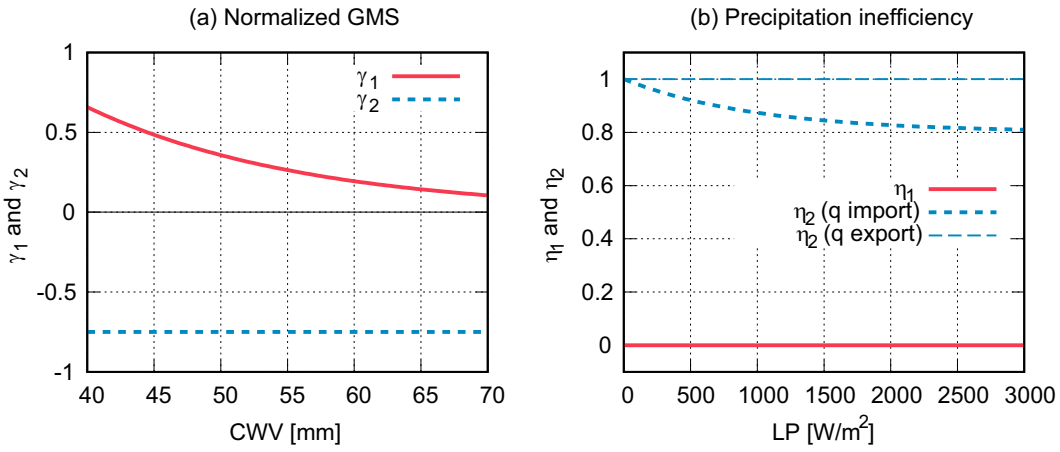

FIG. 3. (a) Normalized GMS as a function of CWV (mm) and (b) precipitation inefficiency as a function of LP (W m^{-2}).

magnitude of the two vertical modes govern the top- or bottom-heaviness in the ω profile as will be detailed later.

A few closure assumptions are applied to the budget equations to make them solvable. First, the horizontal temperature variability is neglected in the MSE storage term,

$$D_t\langle h\rangle' \approx LD_t\langle q\rangle'. \tag{10}$$

This approximation is well justifiable at tropical latitudes (Charney 1963). Second, the vertical MSE advection is related to the vertical moisture advection by invoking a version of the normalized gross moist stability (GMS) (Raymond et al. 2007),

$$\gamma_i \equiv -\frac{\langle\omega_i\partial_p h\rangle'}{L\langle\omega_i\partial_p q\rangle'}, \tag{11}$$

where i (=1, 2) refers to the vertical modes. Using Eqs. (10) and (11), MSE is replaced by the vapor mixing ratio in the budget Eqs. (7) and (8) as

$$D_t\langle q\rangle' + \langle\omega_1\partial_p q\rangle' + \langle\omega_2\partial_p q\rangle' = -P, \tag{12}$$

$$LD_t\langle q\rangle' - \gamma_1 L\langle\omega_1\partial_p q\rangle' - \gamma_2 L\langle\omega_2\partial_p q\rangle' = \langle Q_R\rangle'. \tag{13}$$

Finally, the Lagrangian tendency of moisture is parameterized by a prescribed parameter η defined for each of the two modes as

$$D_t\langle q\rangle' = -\eta_1\langle\omega_1\partial_p q\rangle' - \eta_2\langle\omega_2\partial_p q\rangle', \tag{14}$$

or, equivalently,

$$P = -(1-\eta_1)\langle\omega_1\partial_p q\rangle' - (1-\eta_2)\langle\omega_2\partial_p q\rangle'.$$

By design, η_i refers to the proportion of the dynamic moistening by vertical motion that is left behind in the atmosphere without precipitating out (Masunaga and Sumi 2017). In this paper, η_i is called the precipitation inefficiency.

Eliminating the time-derivative terms in Eqs. (12) and (13) with (14), one obtains diagnostic equations for the first- and second-mode components of the column-integrated vertical moisture advection,

$$L\langle\omega_1\partial_p q\rangle' = -\frac{(\gamma_2+\eta_2)LP - (1-\eta_2)\langle Q_R\rangle'}{(\gamma_2+\eta_2)(1-\eta_1) - (\gamma_1+\eta_1)(1-\eta_2)}, \tag{15}$$

$$L\langle\omega_2\partial_p q\rangle' = \frac{(\gamma_1+\eta_1)LP - (1-\eta_1)\langle Q_R\rangle'}{(\gamma_2+\eta_2)(1-\eta_1) - (\gamma_1+\eta_1)(1-\eta_2)}. \tag{16}$$

Equations (15) and (16), driven by precipitation and ACRE on the rhs, have the practical utility that the column moistening owing to vertical motion is driven by satellite-based retrievals of precipitation and ACRE without explicit knowledge of q and ω.

In calculating Eqs. (15) and (16), γ_i and η_i are prescribed by a simple formula. The normalized GMS is given as a function of column water vapor (CWV) or $\langle q\rangle$ (mm),

$$\gamma_1 = 7.55\exp(-0.061\langle q\rangle), \tag{17}$$

$$\gamma_2 = -0.75, \tag{18}$$

derived from a fit to satellite observations of CWV from AMSR-E measurements and radiative heating from the *CloudSat*/*CALIPSO* product (for details, see Masunaga and Mapes 2020). It is noted that the clear-sky component was not explicitly considered in Masunaga and Mapes (2020), but instead, a background state has been set aside in their formulation, in which the first and second baroclinic modes are considered as a perturbation to the background state. The clear-sky and background states are deemed to be practically equivalent to each other in that both represent a quasi-static reference state against which convective dynamics (i.e., the first and second modes) is defined.

The sharp decline of γ_1 with increasing CWV, as visually evident in Fig. 3a, arises from the fact that the low-level import of MSE increases with CWV and hence offsets to a greater degree the upper-level MSE export in the presence of a deep ascent penetrating the troposphere. On the other hand, the vertical advection of MSE is roughly proportional

to that of moisture when vertical motion is confined to low levels, leading to a practically constant value of γ_2. Of particular importance is that γ_2 is negative, implying that the second baroclinic mode has the potential of driving an unstable growth of moist-convective circulation (Raymond et al. 2009) unless, since the GMS as currently defined is based solely on the vertical component, the vertical MSE advection is more than offset by the horizontal advection.

Precipitation inefficiency is also known to have contrasting behaviors between the first and second modes. It was shown by Masunaga and Sumi (2017) using the DYNAMO sounding array data (Johnson and Ciesielski 2013) that the dynamic moistening by a deep, first-mode ascent is nearly entirely consumed as precipitation, whereas hardly so by a shallow ascent. To reflect this, the present work employs their empirical parameterization with simplification,

$$\eta_1 = 0, \quad \text{and} \tag{19}$$

$$\begin{aligned} \eta_2 &= 0.8 + 0.2\exp(-10^{-3}LP), && \text{for } \langle\omega_2\partial_p q\rangle' < 0, \\ \eta_2 &= 1, && \text{for } \langle\omega_2\partial_p q\rangle' \geq 0, \end{aligned} \tag{20}$$

for LP (W m^{-2}). As plotted in Fig. 3b, η_2 slightly decreases from unity as precipitation picks up, accounting for a nonlinearly increasing moisture with intensifying rainfall as found in the literature (e.g., Bretherton et al. 2004; Holloway and Neelin 2009; Masunaga 2012). This formula is implemented where the second-mode ascent moistens the column (i.e., $\langle\omega_2\partial_p q\rangle' < 0$), but otherwise no precipitation is expected to occur and η_2 is fixed at one. The present results are insensitive to details in the characterization of η_1 and η_2 as far as η_1 stays close to zero and η_2 does not deviate too far from unity.

Note that η_2 is conditioned on the sign of $\langle\omega_2\partial_p q\rangle'$, which formally requires the prior knowledge of η_2 in Eq. (16). In practice, $\gamma_2 + \eta_2$ and $1 - \eta_2$ in Eq. (16) are always positive for all possible values of γ_2 and η_2 as given by Eqs. (18) and (20). It follows that the sign of $\langle\omega_2\partial_p q\rangle'$ may be determined uniquely regardless of η_2.

Equations (15) and (16) constitute a simple model to derive conventionally unobservable variables (vertical advection of q and h) from satellite-retrieved parameters (P and $\langle Q_R\rangle$). Key assumptions behind this model and their validity against in situ sounding array data were discussed in depth by Masunaga and Sumi (2017). They found that the observations overall support the mode-specific precipitation inefficiency (η_1 and η_2) and GMS (γ_1 and γ_2) as currently assumed. The same ideas were later applied with updates to the model of Masunaga and Mapes (2020), which was demonstrated to capture fundamental behaviors in observations.

b. Data

The diagnostic equations [Eqs. (15) and (16)] require surface precipitation both inside and outside the PSs (see section 2 for the definition of PS). Surface precipitation is taken from the IMERG v6 dataset (Huffman et al. 2020). CRE integrated over height $\langle Q_R\rangle'$ is obtained from the Clouds and the Earth's Radiant Energy System (CERES) Synoptic 1° (SYN1deg) data product (Doelling et al. 2016). The CERES SYN1deg product is an hourly, 1° × 1° gridded dataset of the radiative flux fields in the all- and clear-sky atmospheres, derived with the cloud and aerosol observations from GEO and LEO satellite imagers and calibrated to the TOA fluxes from the CERES instruments. In the CERES SYN1deg algorithm, the clear-sky radiance is obtained from radiative transfer calculations with all clouds removed under the otherwise identical atmospheric condition to the all-sky radiance. CWV taken from the hourly fifth major global reanalysis produced by ECMWF (ERA5) data (Hersbach et al. 2020) is used for evaluating γ_1 in Eq. (17). All the variables are averaged to a common 1° × 1° grid across the global tropics from 20°S to 20°N and interpolated over time to half-hourly steps during the whole 2 years of 2007 and 2008.

c. Adaptive domain

The aim of the present budget analysis is to assess the net thermodynamic effects of moist convection on the atmospheric environment of O(100–1000) km in horizontal scale. This line of research has been an area of active interest in tropical meteorology, originating from early work based on field campaign soundings (e.g., Yanai et al. 1973). A geographically fixed array of observations, however, is impractical for applications to the Lagrangian tracking of migrating clouds. This study instead introduces an *adaptive domain* or a study domain varying in size and location as it chases after moving convective systems.

An adaptive domain is defined as the minimum longitude × latitude rectangle enclosing each PS from the IMERG-CT database. As such, grid pixels in the vicinity of a PS are included together with the PS itself as part of the large-scale environment constituted of both raining and rain-free components. If multiple PSs from the same family (see section 2a for definition) emerge in the same snapshot, the minimum rectangle is adjusted so that it encompasses all those PSs at a time. This operation prevents any adaptive domain from being divided into multiple subdomains nor absorbed into another domain for a given PS family throughout its lifetime. The adaptive domains are updated every half hour to adjust themselves to deforming PSs as they move. The four sides of a domain are required to be a multiple of 1° in longitude and latitude, so the domain precisely fits in a block of 1° × 1° grid boxes. Figure 4 schematically illustrates an adaptive domain with a PS embedded inside.

The adaptive domain area can greatly exceed the enclosed PS area when the PS is heavily elongated and/or split into separate systems. To assess the impact of such cases on the composite statistics, a test analysis was run with the "outlier" cases excluded in which the areal ratio of PS to the surrounding adaptive domain is lower than a certain threshold, say, 30%. By exclusion of these events in which precipitation tends to be heavily diluted out, the domain-averaged precipitation composited from the remaining samples is found to be somewhat higher than in the control case. The key results otherwise turn out to be practically unchanged (not shown).

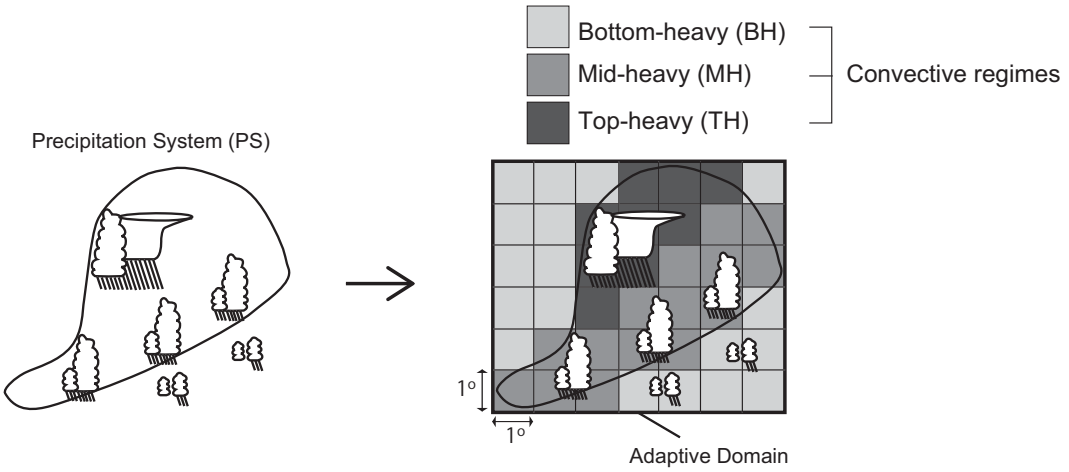

FIG. 4. An example schematic of the adaptive domain (see section 3c) and convective regimes embedded in the domain (section 3d).

d. *Bottom-heavy, midheavy, and top-heavy regimes*

The net export (or import when the sign is reversed) of moisture and MSE is a useful measure of the thermodynamic consequences of vertical motion, founding the basis of three *convective regimes* summarized in Fig. 5. The column-integrated moisture export and MSE export are obtained by combining the first two baroclinic modes,

$$\text{moisture export}: \ \langle \omega \partial_p q \rangle' = \langle \omega_1 \partial_p q \rangle' + \langle \omega_2 \partial_p q \rangle', \tag{21}$$

$$\text{MSE export}: \langle \omega \partial_p h \rangle' = -\gamma_1 L \langle \omega_1 \partial_p q \rangle' - \gamma_2 L \langle \omega_2 \partial_p q \rangle'. \tag{22}$$

Three convective regimes[1] are diagnosed depending on the sign of $\langle \omega \partial_p q \rangle'$ and $\langle \omega \partial_p h \rangle'$. Considered first is the "positive" second baroclinic mode, where the mode is assigned a positive sign when comprising a low-level ascent and an upper-level subsidence. The positive second baroclinic mode, in tandem with a coexisting first baroclinic ascent, gives rise to a very bottom-heavy ω profile with a layer of updraft confined mostly to the lower troposphere. A low-level convergence and a midlevel divergence accompanying this shallow circulation would import both moisture and MSE into the atmospheric column, that is, $\langle \omega \partial_p q \rangle' < 0$ and $\langle \omega \partial_p h \rangle' < 0$. This case is classified into the *bottom-heavy* regime. Although deep, vigorous convection is unlikely to dominate the bottom-heavy regime, a combined effect of the moisture and MSE imports, implying a negative GMS, potentially triggers a rapid growth of moist convection (Raymond et al. 2009).

The *midheavy* regime arises when the layer of updraft develops so deep that it brings about a divergence in the upper troposphere. This is associated with a net export of the column MSE while importing moisture into the column, that is, $\langle \omega \partial_p q \rangle' < 0$ and $\langle \omega \partial_p h \rangle' < 0$. A caveat is that the sign of $\langle \omega \partial_p h \rangle'$ depends on a delicate balance between the lower-tropospheric convergence and upper-tropospheric divergence of MSE, which can be individually large but nearly cancel each other out in a vigorous deep ascent. The resulting smallness of $\langle \omega \partial_p h \rangle'$ would make horizontal MSE advection dominant over the vertical component in the *Eulerian* column import of MSE. It is reminded that the horizontal advection does not explicitly appear in the Lagrangian formulation of the MSE budget [Eq. (5)], formally allowing that the column import and export of MSE are differentiated depending solely on the sign of $\langle \omega \partial_p h \rangle'$.

The vertical motion structure turns into a more top-heavy profile as the negative second mode, made up of an updraft aloft and a downdraft below, comes into play. A midlevel convergence sandwiched by high- and low-level divergences associated with such a top-heavy structure results in a net export of both moisture and MSE from the column. These conditions, $\langle \omega \partial_p q \rangle' < 0$ and $\langle \omega \partial_p h \rangle' < 0$, define the *top-heavy* regime.

Vertical motion is tied with moist convection to the extent that large-scale adiabatic cooling is offset by cloud diabatic heating. Shallow and congestus clouds are presumed to dominate the bottom-heavy regime (Takayabu et al. 2010), while the ω profile in the midheavy regime is accounted for almost exclusively by the first baroclinic mode, ascribable dynamically to deep convective heating (Schumacher et al. 2004). Top-heavy ω profiles, on the other hand, are typical of a mature MCS comprising deep convective cores and extensive stratiform anvils (Mapes and Houze 1995). The characteristic cloud types representative of each regime are included in Fig. 5.

The three convective regimes are identified with Eqs. (21) and (22) on each $1° \times 1°$ pixel (see Fig. 4) making use of the IMERG precipitation, the CERES ACRE, and the ERA5 CWV via Eqs. (15)–(18). This procedure is repeated to all pixels that fall within each adaptive domain. The results are then projected onto the composite life cycle illustrated in section 2b.

[1] The fourth regime, that is, the moisture export combined with the MSE import, rarely occurs in the currently analyzed data and hence is not considered.

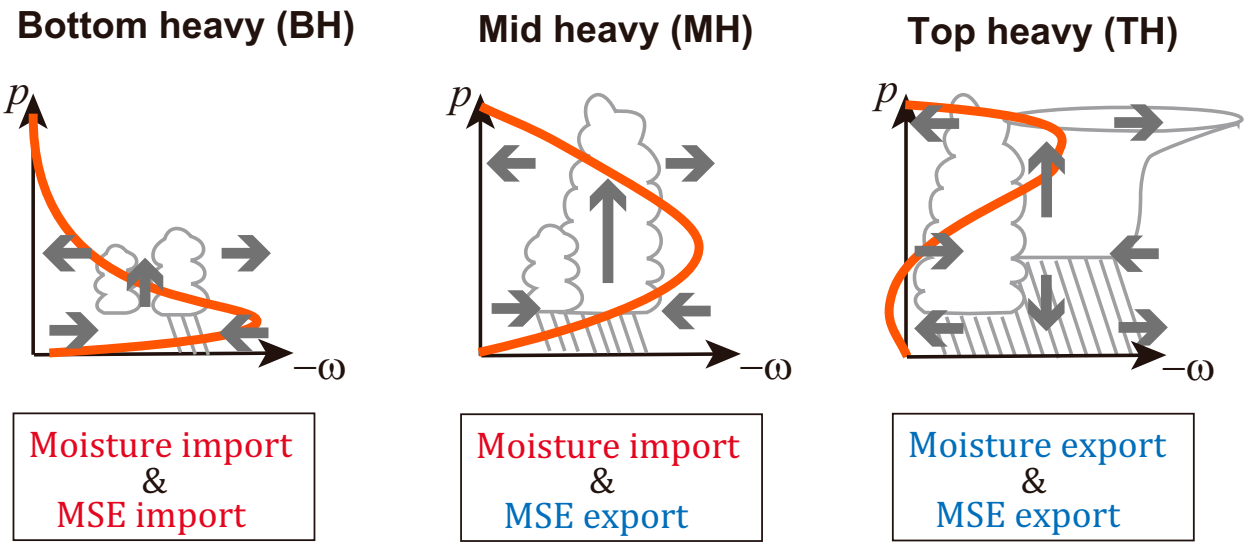

FIG. 5. Schematic illustration of convective regimes, namely, bottom-heavy, midheavy, and top-heavy, based on the sign of moisture/MSE import. Thick curves are the ω profiles typical of each regime, with the sign flipped so that a positive value implies an updraft. Gray arrows indicate the horizontal winds inferred from the ω profile under mass conservation. Cloud cartoons show the cloud type characteristic of each regime (see text for details).

4. Energetics of the Lagrangian life cycle of convection

The main results from the analysis are presented in this section.

a. *Phase diagram of convective regimes*

It follows from Eqs. (15)–(22) that the column-integrated moisture and MSE exports are determined once precipitation (LP) and ACRE ($\langle Q_R \rangle'$) are given. Figure 6a shows the column moisture import mapped onto the LP–$\langle Q_R \rangle'$ plane as derived from Eqs. (15)–(22). CWV must be known to estimate γ_1 by Eq. (17), so the 2-yr mean CWV projected onto the LP–$\langle Q_R \rangle'$ plane is first constructed using the same datasets as employed in the analysis (section 2b). In general, moisture is imported into an atmospheric column where ACRE is large while exported for smaller ACREs, with the boundary in between shifting to a higher ACRE as precipitation increases. It is expected from Eqs. (15) and (16) that the contours would be linear if γ_i and η_i were constant, but in reality, they are heavily curved. This arises primarily from the CWV dependence of γ_1 in Eq. (17). CWV systematically increases with precipitation (Bretherton et al. 2004) and with ACRE (Masunaga and Bony 2018) in the tropical atmosphere, leading

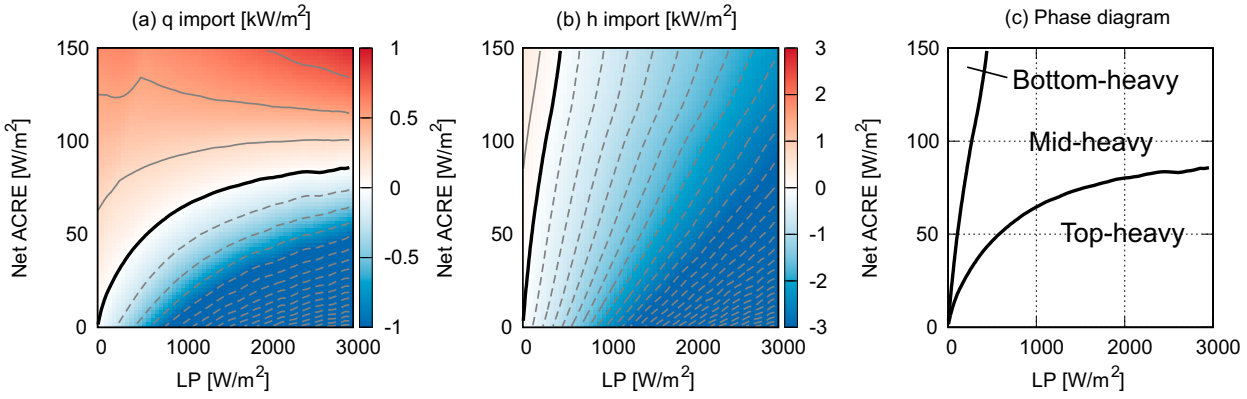

FIG. 6. (a) The column-integrated moisture import $\langle \omega \partial_p q \rangle'$ derived from Eqs. (15)–(22) as a function of precipitation (LP; W m^{-2}) and ACRE ($\langle Q_R \rangle'$; W m^{-2}). The moisture import (export) (in kW m^{-2}) is shaded in red (blue), overlaid by solid (dashed) contours at an interval of 0.25 kW m^{-2}. The thick curve depicts the zero contour. (b) As in (a), but for the MSE import and export. (c) Phase diagram as derived from (a) and (b).

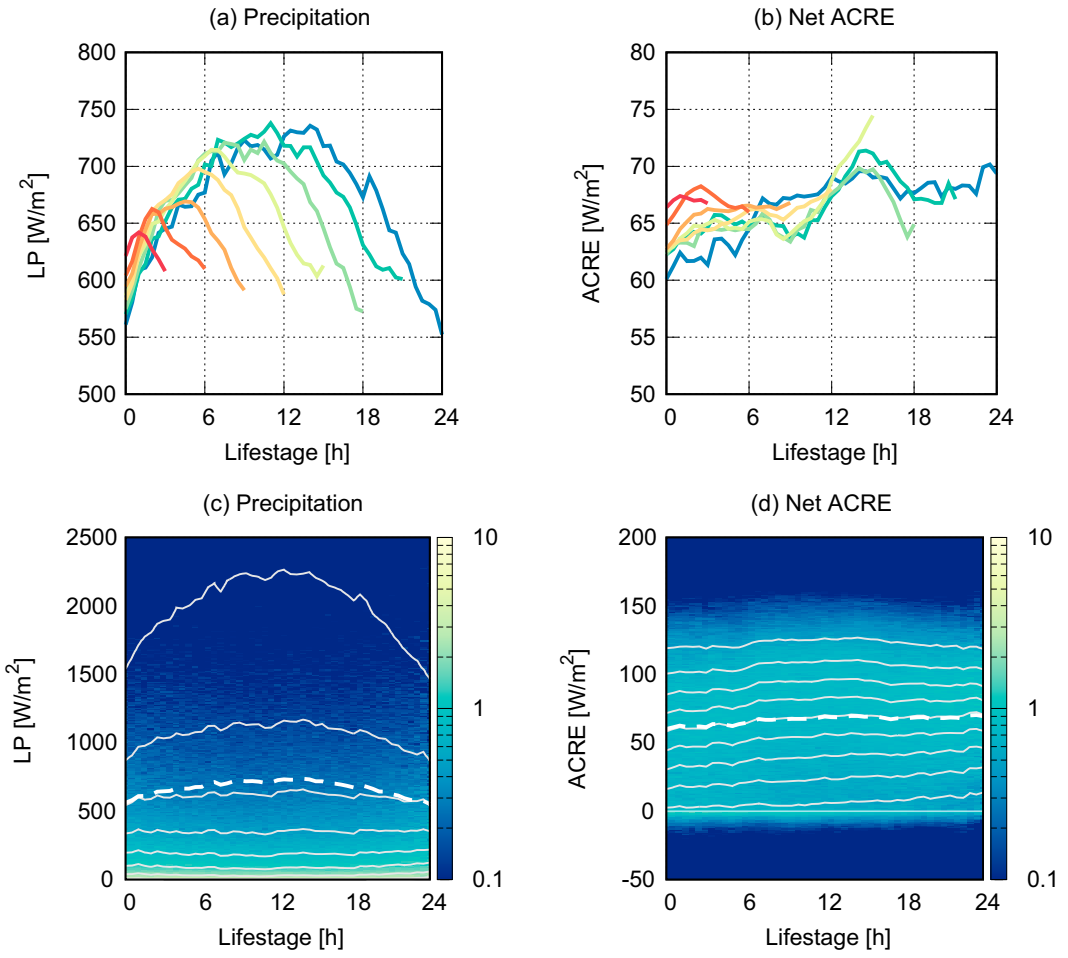

FIG. 7. The composite life cycle of domain-averaged (a) precipitation (W m^{-2}) and (b) ACRE (W m^{-2}), where different curves represent different lifetimes (cf. Table 1 and Fig. 1). The composite life cycle of 1°-scale (c) precipitation and (d) ACRE in PDF (shaded) and cumulative PDF (contoured every 10 percentiles from the 10th to the 90th) with the domain average overlaid (dashed) for reference. Only the lifetime of 24 h is shown for visual clarity.

to a gradient of γ_1 in the precipitation–CRE plane. The P dependence of η_2 also has an effect of distorting the contours, although only to a lesser extent, as the effect is confined to near the upper-left corner of the plot.

A net import of MSE occurs when precipitation is relatively weak and ACRE is large, but otherwise MSE is exported out of the column (Fig. 6b). Combining Figs. 6a and 6b, one obtains the "phase diagram" of the bottom-, mid-, and top-heavy regimes mapped on the LP–$\langle Q_R \rangle'$ plane (Fig. 6c). The bottom- and midheavy regimes are partitioned by the curve on which the MSE import vanishes, while the mid- and top-heavy regimes are separated where the moisture import gives way to the export. This phase diagram serves as a quick reference (in a statistical sense) for finding out which of the three regimes a given observation finds itself in and for predicting when one regime transitions to another as precipitation and ACRE change over time.

b. *Composite life cycle*

The composite life cycle of precipitation and ACRE is plotted in Fig. 7. The evolution of precipitation (Fig. 7a) is by construction parallel to the PS-averaged precipitation shown earlier in Fig. 2a, except that spatial averaging is applied to the adaptive domain containing the environment as well as the PSs it surrounds. A bell-shaped curve of precipitation is absent in ACRE (Fig. 7b), indicative of relatively thin anvil clouds that extend beyond the raining cores toward the end of the life cycle (Protopapadaki et al. 2017), masking the variability intrinsic to precipitation. Precipitation and ACRE span the ranges of 550–750 and 60–70 W m^{-2}, respectively, during the composite life cycle, which may appear to be confined in a somewhat limited parameter space when projected on the phase diagram (Fig. 6c). It is noted, however, that the pixel-by-pixel PDFs of precipitation and ACRE are each spread over a much wider range, skewed toward small values for precipitation (Fig. 7c) while distributed more or less symmetrically about the mean for ACRE (Fig. 7d). The evolutionary tracks of individual events would thus have a broad swath sweeping through the phase diagram when remapped on the LP–ACRE plane.

Among the factors responsible for the statistical spread in the PS properties is diurnal cycle. The composite evolution of

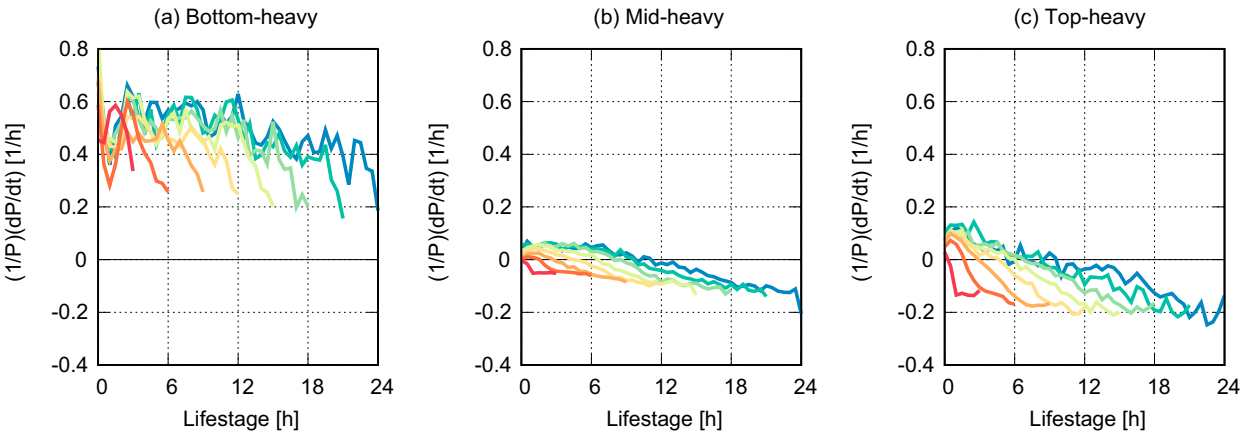

FIG. 8. The composite life cycle of the precipitation growth rate (h^{-1}) for the (a) bottom-heavy regime, (b) midheavy regime, and (c) top-heavy regime. Different curves represent different lifetimes (cf. Table 1 and Fig. 1). See text for a detailed definition of the precipitation growth rate.

ACRE broken down into different local times experiences salient diurnal variability, especially in the shortwave component as expected (Fig. S2). The diurnal variation, however, is largely averaged out when all local times are combined together.

To glimpse the dynamics unique to each convective regime, the domain-averaged precipitation growth rate for a regime R is examined by

$$\left.\overline{\frac{1}{P}\frac{dP}{dt}}(t)\right|^{R} \approx \frac{1}{\sum_{j\in R}\cos y_j}\sum_{j\in R}\frac{1}{P_j(t)}\frac{P_j(t+\Delta t)-P_j(t)}{\Delta t}\cos y_j, \quad (23)$$

where the subscript j refers to a block of $1^\circ \times 1^\circ$ grid pixels within the adaptive domain, y_j is the latitude of the jth grid pixel, and t is the life stage in hours with Δt being the temporal interval fixed at half an hour. The regime R is diagnosed at the life stage of t in Eq. (23) regardless of whether the grid pixel evolves into another regime at $t + \Delta t$. If the grid pixel falls outside the updated adaptive domain at $t + \Delta t$, however, the precipitation growth rate for that grid pixel is removed from the statistics.

Figure 8 shows the composite life cycle of the precipitation growth rate. The growth rate consistently stays positive in the bottom-heavy regime (Fig. 8a), as predicted from the negativeness of GMS intrinsic to a very bottom-heavy ω profile. In contrast, the precipitation growth rate remains positive only in the first half of the lifetime before turning to negative during the rest of life cycle in the midheavy regime, with its magnitude remaining small throughout (Fig. 8b). The decaying phase begins even earlier and is more prominently negative in the precipitation growth rate for the top-heavy regime (Fig. 8c). This is physically plausible in that moist convection is expected to be no longer dynamically sustainable as the atmosphere exports both moisture and MSE in the top-heavy regime.

Less expectedly, however, the life cycle progresses without accompanying any appreciable shift in occurrence from regime to regime. The relative occurrence of each regime is computed at every life stage as

$$f^R(t) = \frac{\sum_{j\in R}\cos y_j}{\sum_{j}\cos y_j}, \quad (24)$$

where the summation in the denominator is applied to all grid pixels within the adaptive domain. The composite life cycle of the regime-by-regime occurrence is shown in Fig. 9. The regime occurrence is found to be surprisingly flat over time regardless of lifetime, setting aside a barely discernible increase for the bottom-heavy regime and a subtle decrease for the top-heavy regime. It is indicated that the Lagrangian evolution of precipitation as we have seen does not involve any noticeable "regime shift" as one might naively anticipate from the conventional scenario of the convective life cycle.

Figure 10 shows the PDF of vertically integrated vertical moisture advection ($-L\langle\omega\partial_p q\rangle'$) and vertical MSE advection ($-\langle\omega\partial_p h\rangle'$). The probability distribution is nearly invariant over time except where moisture import exceeds 90% in cumulative PDF (the uppermost contour in Fig. 10a) and where MSE export is exceptionally large (below 10% or the lowermost contour in Fig. 10b). Recalling that the sign of these variables is diagnosed to define the convective regimes, one finds that the flatness of the convective regime occurrence (Fig. 9) originates from the quasi-steadiness in the statistical distribution of the column processes.

The results above do not necessarily imply that each regime remains "frozen" in itself throughout the life cycle. Figure 11 illustrates what is actually taking place behind the seemingly quasi-static evolution in light of the transition rate from one regime to another,

$$\lambda^{R\to R'}(t) = \frac{\sum_{j\in R\to R'}\cos y_j}{\sum_{j}\cos y_j}, \quad (25)$$

where $R \to R'$ stands for the pixels that belong to the regime R at t but transition to another regime R' at $t + \Delta t$. By

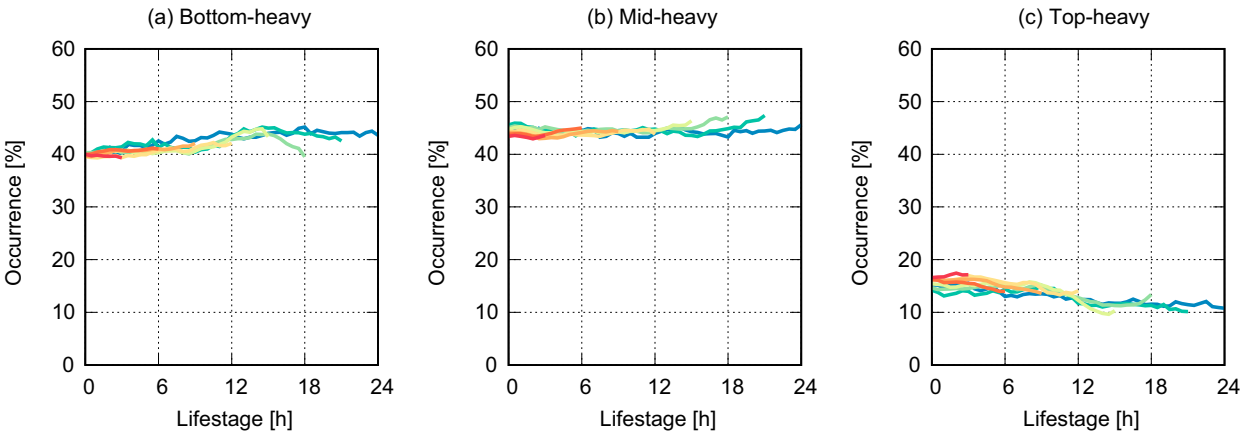

FIG. 9. As in Fig. 8, but for the relative occurrence (%) of each regime.

construction, the rate of temporal change in the regime occurrence is related to the transition ratios as

$$\frac{df^{\mathrm{BH}}}{dt} = (\lambda^{\mathrm{MH}\to\mathrm{BH}} - \lambda^{\mathrm{BH}\to\mathrm{MH}}) + (\lambda^{\mathrm{TH}\to\mathrm{BH}} - \lambda^{\mathrm{BH}\to\mathrm{TH}}) + \sigma^{\mathrm{BH}}, \tag{26}$$

$$\frac{df^{\mathrm{MH}}}{dt} = (\lambda^{\mathrm{TH}\to\mathrm{MH}} - \lambda^{\mathrm{MH}\to\mathrm{TH}}) + (\lambda^{\mathrm{BH}\to\mathrm{MH}} - \lambda^{\mathrm{MH}\to\mathrm{BH}}) + \sigma^{\mathrm{MH}}, \tag{27}$$

$$\frac{df^{\mathrm{TH}}}{dt} = (\lambda^{\mathrm{BH}\to\mathrm{TH}} - \lambda^{\mathrm{TH}\to\mathrm{BH}}) + (\lambda^{\mathrm{MH}\to\mathrm{TH}} - \lambda^{\mathrm{TH}\to\mathrm{MH}}) + \sigma^{\mathrm{TH}}, \tag{28}$$

where BH, MH, and TH denote bottom-heavy, midheavy, and top-heavy, respectively. The last term σ^R summarizes the source and sink arising from the pixels emerging into or disappearing from the adaptive domain as the PS migrates and expands/shrinks as time proceeds from t to $t + \Delta t$. In practice, the adaptive domain only barely moves over a time step of 30 min given a typical migration speed of 10 m s^{-1}. For ease of discussion, the σ^R terms are not considered from now on.

Figure 11a shows a pair of transition rates inside the first parenthesis in Eq. (26). The transition rate from midheavy to bottom-heavy stays around 8% until dropping down toward the end of the life cycle. This is, however, counteracted almost precisely by the inverse transition. The transition rates from top-heavy to midheavy (Fig. 11b) and from bottom-heavy to top-heavy (Fig. 11c) share the common feature that the transitions in opposite directions are virtually a mirror image to the other. It follows that the regime-to-regime transitions largely cancel out when combined into a pair within each parenthesis in Eqs. (26)–(28). These cancellations mathematically explain why the occurrence of each regime is devoid of any notable

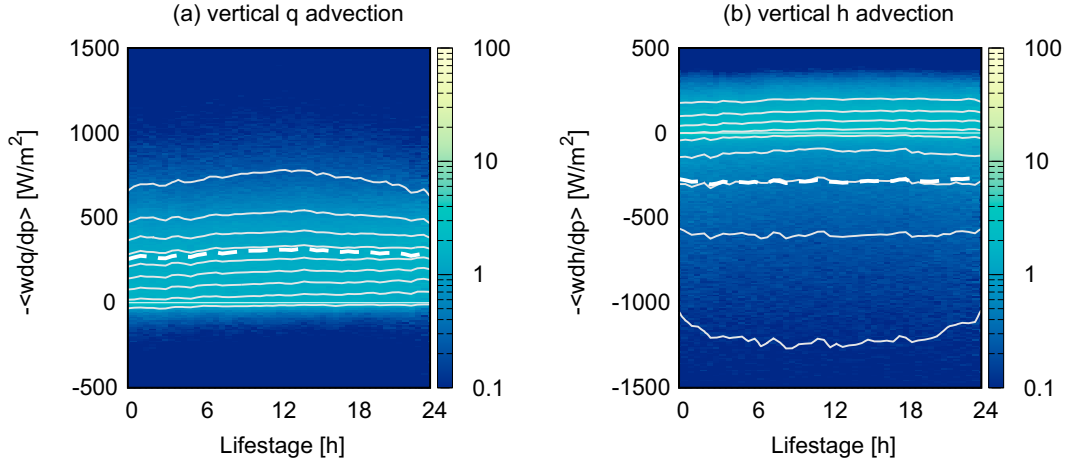

FIG. 10. (a) The composite life cycle of 1°-scale vertically integrated vertical moisture advection $-L\langle\omega\partial_p q\rangle'$ in PDF (shaded) and cumulative PDF (contoured every 10 percentiles from the 10th to the 90th) with the domain average overlaid (dashed) for reference. Positive (negative) values mean a moisture import into (export out of) the column. Only the lifetime of 24 h is shown for visual clarity. (b) As in (a), but for vertical MSE advection $-\langle\omega\partial_p h\rangle'$.

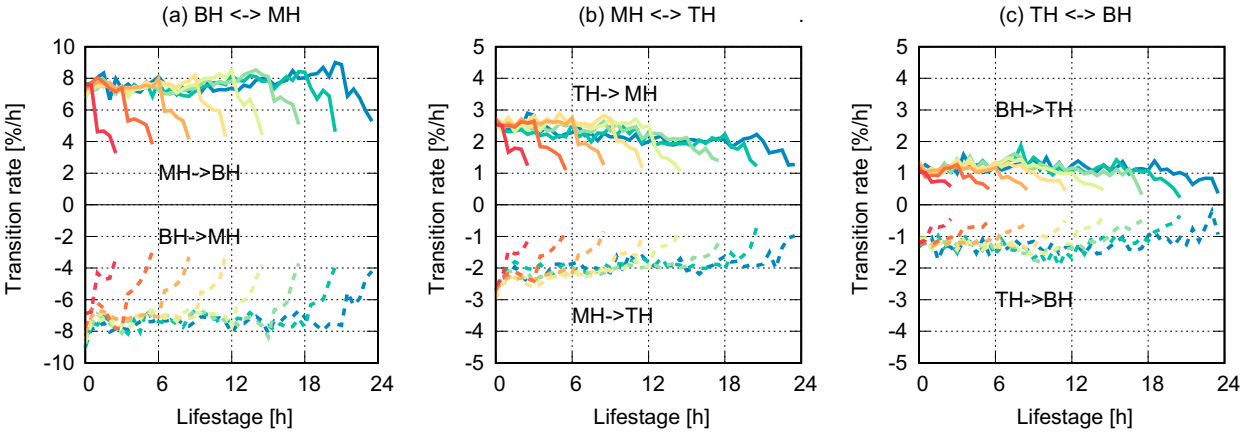

FIG. 11. The composite life cycle of the transition rate (% h^{-1}) between two selected regimes: (a) bottom-heavy and midheavy, (b) midheavy and top-heavy, and (c) top-heavy and bottom-heavy. Different curves represent different lifetimes (cf. Table 1 and Fig. 1). See text for a detailed definition of the transition rates.

temporal evolution (Fig. 9), despite the fact that transitions are active at all times. This result leads to a somewhat surprising conclusion that the three convective regimes are in dynamic equilibrium throughout the Lagrangian life cycle of moving convective systems rather than evolving monotonically from one stage to the next.

5. Discussion

It was discussed near the end of section 2 that a plateau in the maximum-to-average precipitation ratio (Fig. 2c) might imply that the fractional cover of vigorous convective cores in an MCS should be nearly invariant over a span of time. This speculation agrees with the current result in which the relative occurrence of each convective regime including the midheavy, relevant to deep convective heating, stays practically constant (Fig. 9).

Figure 12 shows the precipitation breakdown into the three convective regimes,

$$P^R(t) = \frac{\sum_{j\in R} P_j \cos y_j}{\sum_{j\in R} \cos y_j}. \tag{29}$$

The midheavy regime consistently produces more intense rainfall than the other regimes, making a major contribution to the total precipitation. The predominance of the midheavy regime, backed up by its bell-shaped evolutionary pattern reminiscent of the PS-averaged precipitation (Fig. 2a), supports the presumption for Eq. (3), namely, $P_c \gg P_s$.

The population of different cloud types is known in the literature to evolve systematically during the Lagrangian life cycle of convection. Regardless of spectral windows in use such as infrared brightness temperature (Machado et al. 1998), infrared and visible radiances (Luo and Rossow 2004), and infrared split-window channels (Inoue et al. 2009), these studies all agree that deep convective cores initially dominating the cloud system gradually give way to cirrus clouds that eventually thin out toward the end of the life cycle. It is not entirely clear how to reconcile the apparent contradiction between the monotonic progression of cloud population and the dynamic equilibrium among convective regimes. Among possible explanations is that every $1^\circ \times 1^\circ$ grid box would contain multiple types of clouds at a time, hindering a specific cloud type from mapping uniquely onto a certain convective regime.

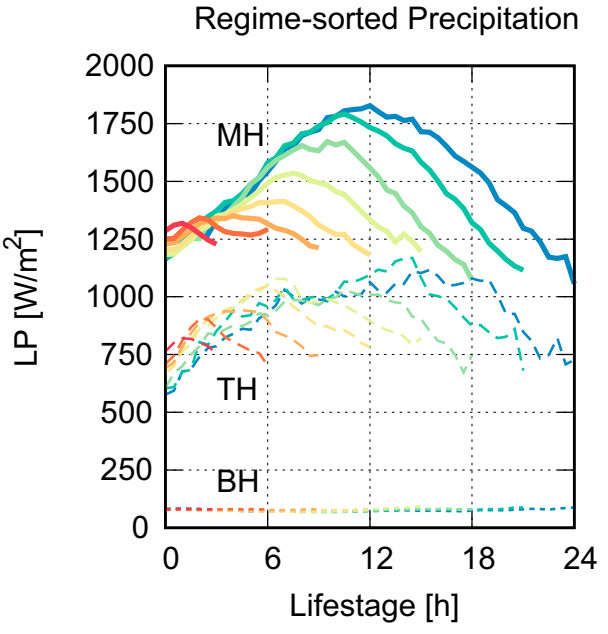

FIG. 12. The composite life cycle of precipitation (W m^{-2}) separated by different convective regimes of bottom-heavy (dotted), midheavy (solid), and top-heavy (dashed). Different curves represent different lifetimes (cf. Table 1 and Fig. 1).

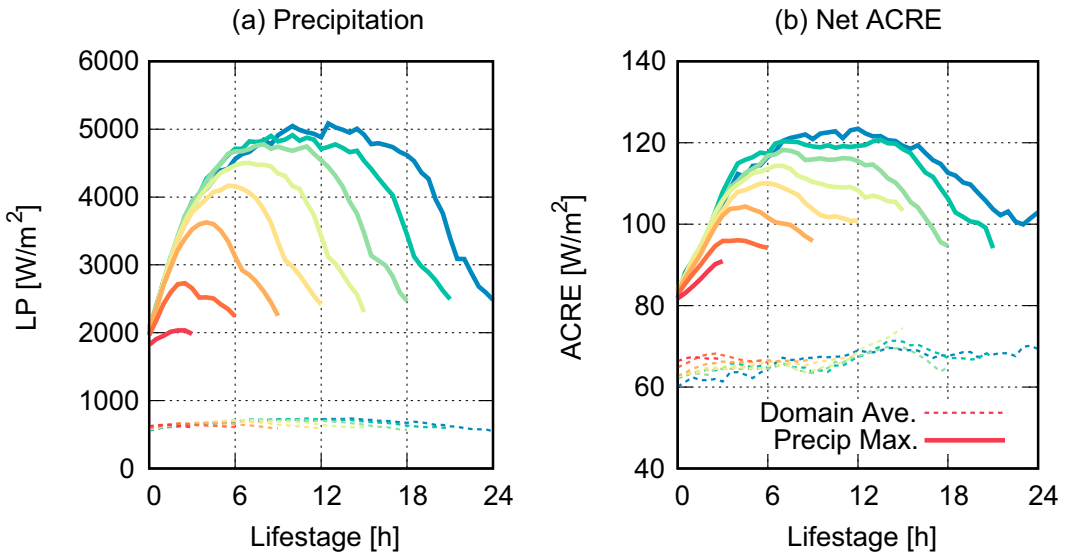

FIG. 13. The composite life cycle of (a) the domain-maximum precipitation (solid; W m^{-2}) and (b) the ACRE cosampled with the domain-maximum precipitation (solid; W m^{-2}). The domain-averaged precipitation and ACRE are reproduced from Fig. 7 (dashed) in each panel for comparison. Different curves represent different lifetimes (cf. Table 1 and Fig. 1).

More importantly, the convective regimes defined in terms of the ω top-heaviness are different in nature from the cloud regimes or weather states identified from the cloud properties (Jakob and Tselioudis 2003; Rossow et al. 2005). Nonprecipitating clouds such as cirrus clouds, for instance, are not a major explanatory factor to differentiate the ω profiles as illustrated in Fig. 5. Precipitating clouds are more likely linked to large-scale dynamics, but this linkage is largely left unexplored in observations of the convective life cycle. A notable exception is the latent heating profiles from the GPM DPR product analyzed by Elsaesser et al. (2022), which were found not to change drastically in top-heaviness during the lifetime (see their Fig. 2). The stability of heating structure is physically consistent with the invariance in the fractional occurrence of each convective regime (Fig. 9).

A fundamental question yet to be addressed is how the midheavy precipitation intensifies and dissipates (Fig. 12). The midheavy regime by definition has a positive GMS (section 3d), in which case precipitation is tightly coupled with the diabatic forcing to the atmosphere (Neelin and Held 1987). This is proven by combining Eqs. (7) and (8) under the steady-state approximation ($D_t \approx 0$) into

$$LP \approx -L\langle \omega \partial_p q \rangle' \approx \frac{\langle Q_R \rangle'}{\gamma}, \tag{30}$$

where γ is the nondecomposed normalized GMS [cf. Eq. (11)],

$$\gamma \equiv -\frac{\langle \omega \partial_p h \rangle'}{L\langle \omega \partial_p q \rangle'}.$$

It is inferred from Eq. (30) that precipitation varies in proportion to the diabatic forcing, which is reduced to ACRE in the current formulation of the MSE budget Eq. (8), to the extent that γ is deemed as invariant. The domain-mean ACRE, however, is not quite in parallel with the bell-shaped curve of precipitation as observed (Fig. 7b). This qualitative discrepancy may not be entirely unexpected, given that the bell shape is attributed mainly to a relatively small number of intense events as evidenced by the cumulative PDF of precipitation shown by Fig. 7c.

Figure 13 presents the composite pattern of the domain-maximum precipitation and the cosampled ACRE. ACRE is found to exhibit a salient bell-shaped feature when sampled exclusively with heavy precipitation, now matching the theoretical expectation of Eq. (30). For $LP \sim 5000$ W m^{-2} (Fig. 13a) and $\langle Q_R \rangle' \sim 120$ W m^{-2} (Fig. 13b), γ is estimated from Eq. (30) to be ~0.024. This value is even smaller than γ_1 could be (see Fig. 3a), necessitating a more bottom-heavy ω profile than the first-baroclinic mode typical of the midheavy regime. Heavy precipitation associated with such a bottom-heavy ascent is interpreted as a burst of convection invigorated as the bottom-heavy regime, which by definition has a negative GMS and potentially nurtures a self-sustaining growth of convection, transitions to the midheavy regime. This might be among the processes lying behind the fact that the heaviest rains tend to be produced not by the deepest convection but by relatively bottom-heavy clouds (Hamada et al. 2015).

To examine the time scale of this process, let us consider a hypothetical system that initially consists only of the bottom-heavy regime developing into the midheavy regime. The rate of change in the midheavy occurrence in Eq. (27) is simplified as

$$\frac{df^{\mathrm{MH}}}{dt} = \lambda^{\mathrm{BH}\to\mathrm{MH}}, \tag{31}$$

assuming that all other processes are absent. The relaxation time with respect to this transition is defined from Eq. (31) as

$$\tau_{\mathrm{MH}}^{\mathrm{BH}\rightarrow\mathrm{MH}} \sim \frac{f^{\mathrm{MH}}}{\lambda^{\mathrm{BH}\rightarrow\mathrm{MH}}}. \tag{32}$$

If the midheavy regime then transitions into the top-heavy regime, the relaxation time regarding this second transition is estimated similarly as

$$\tau_{\mathrm{MH}}^{\mathrm{MH}\rightarrow\mathrm{TH}} \sim \frac{f^{\mathrm{MH}}}{\lambda^{\mathrm{MH}\rightarrow\mathrm{TH}}}. \tag{33}$$

It is found from Figs. 9b and 11a that $f^{\mathrm{MH}} \approx 40\%\ \mathrm{h}^{-1}$ and $\lambda^{\mathrm{BK}\rightarrow\mathrm{MH}} \approx 8\%\ \mathrm{h}^{-1}$ at $t = 0$. Substituting these estimates into Eq. (32), one obtains

$$\tau_{\mathrm{MH}}^{\mathrm{BH}\rightarrow\mathrm{MH}} \sim 5\,\mathrm{h}. \tag{34}$$

Applying $\lambda^{\mathrm{MH}\rightarrow\mathrm{TH}} \approx 2\%\ \mathrm{h}^{-1}$ (Fig. 11b) to Eq. (33) leads to

$$\tau_{\mathrm{MH}}^{\mathrm{MH}\rightarrow\mathrm{TH}} \sim 20\,\mathrm{h}. \tag{35}$$

Equation (34) suggests that the transition from the bottom-heavy regime, supposedly a feeding agent for convective intensification, takes the relaxation time of 5 h before substantially influencing the midheavy regime through the equilibrating processes. This estimate is roughly consistent with the time it takes for the maximum-to-average precipitation ratio to climb up before reaching a plateau (Fig. 2c). The relaxation time $\tau_{\mathrm{MH}}^{\mathrm{BH}\rightarrow\mathrm{MH}}$ is hence a measure of the time required for the midheavy regime to "metabolize" itself through the transition with the bottom-heavy regime. The second time scale of 20 h in Eq. (35) is longer than the first, suggesting in theory that the system-maximum precipitation gives way to the decaying stage more slowly than the earlier intensifying stage. This is confirmed by the gradual decline of the maximum-to-average ratio toward the end of the life cycle (Fig. 2c). Note that equilibration is expected to be completed only when the relaxation time is shorter than the system lifetime.

The dynamic equilibrium scenario in the Lagrangian convective life cycle marks a contrast with the conventional scenario of MCS evolution built largely on the Eulerian perspective. The two pictures may seem intuitively inconsistent but can be reconciled analogically in light of the typical life cycle of a long-lived squall line as an example. A propagating squall line projected on Eulerian coordinates begins with a line of convective clouds entering the study domain and ends with a trailing stratiform anvil eventually leaving out of the domain, depicting a life cycle lasting no longer than the time that takes for the system to pass through the domain. In contrast, the Lagrangian picture is more of a quasi-static system persisting for an extended period of time, resulting from a sequence of short-lived cells being renewed continuously as they move. This stationarity in the Lagrangian framework may be translated into a state of dynamic equilibrium when interpreted in the context of large-scale thermodynamics.

The merging and splitting of clouds are a potential source of ambiguity. The dynamic equilibrium as pictured above is built on the assumption that regime-to-regime transitions occur within each PS, whereas this premise is potentially complicated by multiple concurrent PSs before merger or after splitting that are mixed together into the composite evolution. To look into this, a sensitivity test is run with the selected samples that consist exclusively of the life stages at which only a single PS exists. This test case is intended to see to what extent composite statistics may be distorted by coexisting PSs. As shown in Fig. S3, the evolution remains essentially unchanged from Figs. 2 and 9, implying that the merging and splitting unlikely impose a major effect on composite time series.

6. Conclusions

The Lagrangian life cycle of organized moist convection was investigated with focus on the underlying physical processes by tracking migrating precipitation systems and their large-scale environment. The composite evolution analyzed with the IMERG-CT dataset was found to depict an initial pickup and a subsequent decline in both the system mean and maximum precipitations as known in the literature. A lesser-known feature is that the maximum-to-average precipitation ratio exhibits a plateau in between, especially for long-lived systems. The plateau suggests that the fractional cover of localized intense precipitation such as deep convective cores may stay for a certain span of time in the course of the convective life cycle.

In an attempt to explore the mechanism behind these observations, the study domain enclosing tracked precipitation systems was broken down on a $1^\circ \times 1^\circ$ grid basis into the bottom-heavy, midheavy, and top-heavy regimes. Each regime is defined depending on the sign of column moisture/MSE export diagnosed from a water/energy budget analysis forced by the satellite retrievals of precipitation and radiation. In the bottom-heavy regime, an atmospheric column imports both moisture and MSE owing to a very bottom-heavy ω profile, whereas the ω structure is less bottom-heavy in the midheavy regime, resulting in an import of moisture and an export of MSE. Column moisture and MSE are both exported when ω is even top-heavier, which defines the top-heavy regime. As such, these three regimes are intended to separate the strength of moist convection from the thermodynamic perspectives.

A key finding from the regime-sorted composite analysis is that the transition from one regime to another is closely balanced against the inverse process, implying a state of dynamic equilibrium in which the relative occurrence of each regime stays nearly invariant during the whole life cycle. The growth of precipitation toward the peak is arguably activated by a negative GMS intrinsic to the bottom-heavy regime, leading to a burst of convection in the transition from the bottom-heavy to the midheavy regimes. This transition, evaluated with a dimensional analysis to have a relaxation time of about 5 h, takes place as part of the equilibrating processes for systems lasting longer than the relaxation time. This time scale is close to the time taken by the initial rise of the maximum-to-average precipitation ratio before it is settled into a plateau. The more gradual decay of precipitation toward the end of

the life cycle could be interpreted as the transition from the midheavy regime to the top-heavy regime.

Some fundamental aspects of the Lagrangian evolution of convective systems remain to be answered. Key outstanding questions include what determines the timing and magnitude of the precipitation peak during the life cycle and what controls the system lifetime. The analysis method devised in this study will be further refined in future work in an attempt to shed new light on these long-standing problems.

Acknowledgments. The authors greatly appreciate insightful feedback from Johnny Luo on an early version of the manuscript and are grateful to three anonymous reviewers for their thoughtful and helpful comments. HM was supported by the Japan Society for the Promotion of Science (JSPS) Grants-in-Aid for Scientific Research (KAKENHI) 19H01966 and the Japan Science and Technology Agency (JST) Moonshot R&D Program JPMJMS2389. The work of HT was funded by NASA's Atmosphere Observing System under WBS/RTOP:107686/04.02.06.

Data availability statement. The IMERG data are available from Goddard Earth Sciences Data and Information Services Center (GES DISC) (https://disc.gsfc.nasa.gov/datasets/GPM_3IMERGHH_06/summary) (Huffman et al. 2019). The CERES SYN1deg product is provided by NASA Langley Atmospheric Science Data Center (https://asdc.larc.nasa.gov/project/CERES/CER_SYN1deg-1Hour_Terra-Aqua-MODIS_Edition4A) (NASA/LARC/SD/ASDC 2017). The ERA5 CWV data are available from Copernicus Climate Change Service (C3S) Climate Data Store (CDS) (https://cds.climate.copernicus.eu/cdsapp#!/dataset/reanalysis-era5-single-levels) (Hersbach et al. 2023).

REFERENCES

Arakawa, A., and W. H. Schubert, 1974: Interaction of a cumulus cloud ensemble with the large-scale environment. Part I. *J. Atmos. Sci.*, **31**, 674–701, https://doi.org/10.1175/1520-0469(1974)031<0674:IOACCE>2.0.CO;2.

Back, L. E., Z. Hansen, and Z. Handlos, 2017: Estimating vertical motion profile top-heaviness: Reanalysis compared to satellite-based observations and stratiform rain fraction. *J. Atmos. Sci.*, **74**, 855–864, https://doi.org/10.1175/JAS-D-16-0062.1.

Bouniol, D., R. Roca, T. Fiolleau, and D. E. Poan, 2016: Macrophysical, microphysical, and radiative properties of tropical mesoscale convective systems over their life cycle. *J. Climate*, **29**, 3353–3371, https://doi.org/10.1175/JCLI-D-15-0551.1.

——, ——, ——, and P. Raberanto, 2021: Life cycle-resolved observation of radiative properties of mesoscale convective systems. *J. Appl. Meteor. Climatol.*, **60**, 1091–1104, https://doi.org/10.1175/JAMC-D-20-0244.1.

Bretherton, C. S., M. E. Peters, and L. E. Back, 2004: Relationships between water vapor path and precipitation over the tropical oceans. *J. Climate*, **17**, 1517–1528, https://doi.org/10.1175/1520-0442(2004)017<1517:RBWVPA>2.0.CO;2.

Charney, J. G., 1963: A note on large-scale motions in the tropics. *J. Atmos. Sci.*, **20**, 607–609, https://doi.org/10.1175/1520-0469(1963)020<0607:ANOLSM>2.0.CO;2.

Chen, S. S., and R. A. Houze Jr., 1997: Diurnal variation and life-cycle of deep convective systems over the tropical Pacific warm pool. *Quart. J. Roy. Meteor. Soc.*, **123**, 357–388, https://doi.org/10.1002/qj.49712353806.

Chikira, M., 2014: Eastward-propagating intraseasonal oscillation represented by Chikira-Sugiyama cumulus parameterization. Part II: Understanding moisture variation under weak temperature gradient balance. *J. Atmos. Sci.*, **71**, 615–639, https://doi.org/10.1175/JAS-D-13-038.1.

Doelling, D. R., M. Sun, L. T. Nguyen, M. L. Nordeen, C. O. Haney, D. F. Keyes, and P. E. Mlynczak, 2016: Advances in geostationary-derived longwave fluxes for the CERES synoptic (SYN1deg) product. *J. Atmos. Oceanic Technol.*, **33**, 503–521, https://doi.org/10.1175/JTECH-D-15-0147.1.

Elsaesser, G. S., R. Roca, T. Fiolleau, A. D. Del Genio, and J. Wu, 2022: A simple model for tropical convective cloud shield area growth and decay rates informed by geostationary IR, GPM, and Aqua/AIRS satellite data. *J. Geophys. Res. Atmos.*, **127**, e2021JD035599, https://doi.org/10.1029/2021JD035599.

Emanuel, K. A., J. D. Neelin, and C. S. Bretherton, 1994: On large-scale circulations in convecting atmospheres. *Quart. J. Roy. Meteor. Soc.*, **120**, 1111–1143, https://doi.org/10.1002/qj.49712051902.

Feng, Z., X. Dong, B. Xi, C. Schumacher, P. Minnis, and M. Khaiyer, 2011: Top-of-atmosphere radiation budget of convective core/stratiform rain and anvil clouds from deep convective systems. *J. Geophys. Res.*, **116**, D23202, https://doi.org/10.1029/2011JD016451.

——, ——, ——, S. A. McFarlane, A. Kennedy, B. Lin, and P. Minnis, 2012: Life cycle of midlatitude deep convective systems in a Lagrangian framework. *J. Geophys. Res.*, **117**, D23201, https://doi.org/10.1029/2012JD018362.

——, and Coauthors, 2021: A global high-resolution mesoscale convective system database using satellite-derived cloud tops, surface precipitation, and tracking. *J. Geophys. Res. Atmos.*, **126**, e2020JD034202, https://doi.org/10.1029/2020JD034202.

Fiolleau, T., and R. Roca, 2013a: An algorithm for the detection and tracking of tropical mesoscale convective systems using infrared images from geostationary satellite. *IEEE Trans. Geosci. Remote Sens.*, **51**, 4302–4315, https://doi.org/10.1109/TGRS.2012.2227762.

——, and ——, 2013b: Composite life cycle of tropical mesoscale convective systems from geostationary and low Earth orbit satellite observations: Method and sampling considerations. *Quart. J. Roy. Meteor. Soc.*, **139**, 941–953, https://doi.org/10.1002/qj.2174.

Futyan, J. M., and A. D. Del Genio, 2007: Deep convective system evolution over Africa and the tropical Atlantic. *J. Climate*, **20**, 5041–5060, https://doi.org/10.1175/JCLI4297.1.

Hamada, A., Y. N. Takayabu, C. Liu, and E. J. Zipser, 2015: Weak linkage between the heaviest rainfall and tallest storms. *Nat. Commun.*, **6**, 6213, https://doi.org/10.1038/ncomms7213.

Hannah, W. M., B. E. Mapes, and G. S. Elsaesser, 2016: A Lagrangian view of moisture dynamics during DYNAMO. *J. Atmos. Sci.*, **73**, 1967–1985, https://doi.org/10.1175/JAS-D-15-0243.1.

Heikenfeld, M., P. J. Marinescu, M. Christensen, D. Watson-Parris, F. Senf, S. C. van den Heever, and P. Stier, 2019: Tobac 1.2: Towards a flexible framework for tracking and analysis of clouds in diverse datasets. *Geosci. Model Dev.*, **12**, 4551–4570, https://doi.org/10.5194/gmd-12-4551-2019.

Hersbach, H., and Coauthors, 2020: The ERA5 global reanalysis. *Quart. J. Roy. Meteor. Soc.*, **146**, 1999–2049, https://doi.org/10.1002/qj.3803.

——, and Coauthors, 2023: ERA5 hourly data on single levels from 1940 to present. Copernicus Climate Change Service (C3S) Climate Data Store (CDS), accessed 28 March 2024, https://doi.org/10.24381/cds.adbb2d47.

Holloway, C. E., and J. D. Neelin, 2009: Moisture vertical structure, column water vapor, and tropical deep convection. *J. Atmos. Sci.*, **66**, 1665–1683, https://doi.org/10.1175/2008JAS2806.1.

Huffman, G. J., E. F. Stocker, D. T. Bolvin, E. J. Nelkin, and J. Tan, 2019: GPM IMERG final precipitation L3 half hourly 0.1 degree × 0.1 degree V06. Goddard Earth Sciences Data and Information Services Center (GES DISC), accessed 28 March 2024, https://doi.org/10.5067/GPM/IMERG/3B-HH/06.

——, and Coauthors, 2020: Integrated Multi-satellite Retrievals for the Global Precipitation Measurement (GPM) mission (IMERG). *Satellite Precipitation Measurement*, V. Levizzani et al., Eds., Springer International Publishing, 343–353, https://doi.org/10.1007/978-3-030-24568-9_19.

Inoue, K., and L. Back, 2015: Column-integrated moist static energy budget analysis on various time scales during TOGA COARE. *J. Atmos. Sci.*, **72**, 1856–1871, https://doi.org/10.1175/JAS-D-14-0249.1.

——, and ——, 2017: Gross moist stability analysis: Assessment of satellite-based products in the GMS plane. *J. Atmos. Sci.*, **74**, 1819–1837, https://doi.org/10.1175/JAS-D-16-0218.1.

Inoue, T., D. Vila, K. Rajendran, A. Hamada, X. Wu, and L. A. T. Machado, 2009: Life cycle of deep convective systems over the eastern tropical Pacific observed by TRMM and GOES-W. *J. Meteor. Soc. Japan*, **87A**, 381–391, https://doi.org/10.2151/jmsj.87A.381.

Jakob, C., and G. Tselioudis, 2003: Objective identification of cloud regimes in the tropical western Pacific. *Geophys. Res. Lett.*, **30**, 2082, https://doi.org/10.1029/2003GL018367.

Johnson, R. H., and P. E. Ciesielski, 2013: Structure and properties of Madden-Julian Oscillations deduced from DYNAMO sounding arrays. *J. Atmos. Sci.*, **70**, 3157–3179, https://doi.org/10.1175/JAS-D-13-065.1.

Khouider, B., and A. J. Majda, 2006: A simple multicloud parameterization for convectively coupled tropical waves. Part I: Linear analysis. *J. Atmos. Sci.*, **63**, 1308–1323, https://doi.org/10.1175/JAS3677.1.

Kuang, Z., 2008: A moisture-stratiform instability for convectively coupled waves. *J. Atmos. Sci.*, **65**, 834–854, https://doi.org/10.1175/2007JAS2444.1.

Leary, C. A., and R. A. Houze Jr., 1979: The structure and evolution of convection in a tropical cloud cluster. *J. Atmos. Sci.*, **36**, 437–457, https://doi.org/10.1175/1520-0469(1979)036<0437:TSAEOC>2.0.CO;2.

Lin, X., and R. H. Johnson, 1996: Kinematic and thermodynamic characteristics of the flow over the western Pacific warm pool during TOGA COARE. *J. Atmos. Sci.*, **53**, 695–715, https://doi.org/10.1175/1520-0469(1996)053<0695:KATCOT>2.0.CO;2.

Luo, Z., and W. B. Rossow, 2004: Characterizing tropical cirrus life cycle, evolution, and interaction with upper-tropospheric water vapor using Lagrangian trajectory analysis of satellite observations. *J. Climate*, **17**, 4541–4563, https://doi.org/10.1175/3222.1.

Machado, L. A. T., W. B. Rossow, R. L. Guedes, and A. W. Walker, 1998: Life cycle variations of mesoscale convective systems over the Americas. *Mon. Wea. Rev.*, **126**, 1630–1654, https://doi.org/10.1175/1520-0493(1998)126<1630:LCVOMC>2.0.CO;2.

Mapes, B., 2000: Convective inhibition, subgrid-scale triggering energy, and stratiform instability in a toy tropical wave model. *J. Atmos. Sci.*, **57**, 1515–1535, https://doi.org/10.1175/1520-0469(2000)057<1515:CISSTE>2.0.CO;2.

——, and R. A. Houze Jr., 1993: Cloud clusters and superclusters over the oceanic warm pool. *Mon. Wea. Rev.*, **121**, 1398–1416, https://doi.org/10.1175/1520-0493(1993)121<1398:CCASOT>2.0.CO;2.

——, and ——, 1995: Diabatic divergence profiles in western Pacific mesoscale convective systems. *J. Atmos. Sci.*, **52**, 1807–1828, https://doi.org/10.1175/1520-0469(1995)052<1807:DDPIWP>2.0.CO;2.

——, S. Tulich, J. Lin, and P. Zuidema, 2006: The mesoscale convection life cycle: Building block or prototype for large-scale tropical waves? *Dyn. Atmos. Oceans*, **42**, 3–29, https://doi.org/10.1016/j.dynatmoce.2006.03.003.

Masunaga, H., 2012: Short-term versus climatological relationship between precipitation and tropospheric humidity. *J. Climate*, **25**, 7983–7990, https://doi.org/10.1175/JCLI-D-12-00037.1.

——, and T. S. L'Ecuyer, 2014: A mechanism of tropical convection inferred from observed variability in the moist static energy budget. *J. Atmos. Sci.*, **71**, 3747–3766, https://doi.org/10.1175/JAS-D-14-0015.1.

——, and Y. Sumi, 2017: A toy model of tropical convection with a moisture storage closure. *J. Adv. Model. Earth Syst.*, **9**, 647–667, https://doi.org/10.1002/2016MS000855.

——, and S. Bony, 2018: Radiative invigoration of tropical convection by preceding cirrus clouds. *J. Atmos. Sci.*, **75**, 1327–1342, https://doi.org/10.1175/JAS-D-17-0355.1.

——, and B. E. Mapes, 2020: A mechanism for the maintenance of sharp tropical margins. *J. Atmos. Sci.*, **77**, 1181–1197, https://doi.org/10.1175/JAS-D-19-0154.1.

NASA/LARC/SD/ASDC, 2017: CERES and GEO-enhanced TOA, within-atmosphere and surface fluxes, clouds and aerosols 1-hourly Terra-Aqua Edition4A. NASA Langley Atmospheric Science Data Center DAAC, accessed 28 March 2024, https://doi.org/10.5067/TERRA+AQUA/CERES/SYN1DEG-1HOUR_L3.004A.

Neelin, J. D., and I. M. Held, 1987: Modeling tropical convergence based on the moist static energy budget. *Mon. Wea. Rev.*, **115**, 3–12, https://doi.org/10.1175/1520-0493(1987)115<0003:MTCBOT>2.0.CO;2.

Protopapadaki, S. E., C. J. Stubenrauch, and A. G. Feofilov, 2017: Upper tropospheric cloud systems derived from IR sounders: Properties of cirrus anvils in the tropics. *Atmos. Chem. Phys.*, **17**, 3845–3859, https://doi.org/10.5194/acp-17-3845-2017.

Raymond, D. J., S. L. Sessions, and Ž. Fuchs, 2007: A theory for the spinup of tropical depressions. *Quart. J. Roy. Meteor. Soc.*, **133**, 1743–1754, https://doi.org/10.1002/qj.125.

——, ——, A. H. Sobel, and Ž. Fuchs, 2009: The mechanics of gross moist stability. *J. Adv. Model. Earth Syst.*, **1**, 9, https://doi.org/10.3894/JAMES.2009.1.9.

Rossow, W. B., G. Tselioudis, A. Polak, and C. Jakob, 2005: Tropical climate described as a distribution of weather states indicated by distinct mesoscale cloud property mixtures. *Geophys. Res. Lett.*, **32**, L21812, https://doi.org/10.1029/2005GL024584.

Schumacher, C., R. A. Houze Jr., and I. Kraucunas, 2004: The tropical dynamical response to latent heating estimates derived from the TRMM precipitation radar. *J. Atmos. Sci.*, **61**, 1341–1358, https://doi.org/10.1175/1520-0469(2004)061<1341:TTDRTL>2.0.CO;2.

Straub, K. H., and G. N. Kiladis, 2003: The observed structure of convectively coupled Kelvin waves: Comparison with simple models of coupled wave instability. *J. Atmos. Sci.*, **60**, 1655–1668, https://doi.org/10.1175/1520-0469(2003)060<1655:TOSOCC>2.0.CO;2.

Takahashi, H., and Z. J. Luo, 2014: Characterizing tropical overshooting deep convection from joint analysis of CloudSat and geostationary satellite observations. *J. Geophys. Res. Atmos.*, **119**, 112–121, https://doi.org/10.1002/2013JD020972.

——, M. Lebsock, Z. J. Luo, H. Masunaga, and C. Wang, 2021: Detection and tracking of tropical convective storms based on globally gridded precipitation measurements: Algorithm and survey over the tropics. *J. Appl. Meteor. Climatol.*, **60**, 403–421, https://doi.org/10.1175/JAMC-D-20-0171.1.

Takayabu, Y. N., K.-M. Lau, and C.-S. Sui, 1996: Observation of a quasi-2-day wave during TOGA COARE. *Mon. Wea. Rev.*, **124**, 1892–1913, https://doi.org/10.1175/1520-0493(1996)124<1892:OOAQDW>2.0.CO;2.

——, S. Shige, W.-K. Tao, and N. Hirota, 2010: Shallow and deep latent heating modes over tropical oceans observed with TRMM PR spectral latent heating data. *J. Climate*, **23**, 2030–2046, https://doi.org/10.1175/2009JCLI3110.1.

Williams, M., and R. A. Houze Jr., 1987: Satellite-observed characteristics of winter monsoon cloud clusters. *Mon. Wea. Rev.*, **115**, 505–519, https://doi.org/10.1175/1520-0493(1987)115<0505:SOCOWM>2.0.CO;2.

Woodley, W. L., C. G. Griffith, J. S. Griffin, and S. C. Stromatt, 1980: The inference of GATE convective rainfall from SMS-1 imagery. *J. Appl. Meteor.*, **19**, 388–408, https://doi.org/10.1175/1520-0450(1980)019<0388:TIOGCR>2.0.CO;2.

Yanai, M., S. Esbensen, and J.-H. Chu, 1973: Determination of bulk properties of tropical cloud clusters from large-scale heat and moisture budgets. *J. Atmos. Sci.*, **30**, 611–627, https://doi.org/10.1175/1520-0469(1973)030<0611:DOBPOT>2.0.CO;2.